Journal of Quantitative Spectroscopy & Radiative Transfer 310 (2023) 108749

Contents lists available at ScienceDirect

Journal of Quantitative Spectroscopy and Radiative Transfer

journal homepage: www.elsevier.com/locate/jqsrt

Review

Version 5 retrievals for ACE-FTS and ACE-imagers

C.D. Boone [a,*], P.F. Bernath [a,b], M. Lecours [a]

[a] Department of Chemistry, University of Waterloo, 200 University Avenue West, Ontario N2L 3G1, Canada
[b] Department of Chemistry and Biochemistry, Old Dominion University, Norfolk, VA 23529, USA

ARTICLE INFO

Keywords:
Remote sensing
Retrievals

ABSTRACT

A new processing version is described for two instruments on board the Atmospheric Chemistry Experiment satellite: the Fourier transform spectrometer (ACE-FTS) and a pair of filtered imagers. The new processing version fixes issues observed for previous processing versions and updates the spectroscopic database to the most recent information. Three new data products are added: line of sight winds and volume mixing ratios for two molecules: HFC-32 (CH_2F_2) and HOCl. Forward model calculations are updated to account for the finite ACE-FTS field of view. The processing version recommended for scientific analysis is version 5.2 (v5.2), which filters out unphysical results arising from intermittent convergence problems in the software for v5.1.

1. Introduction

The Atmospheric Chemistry Experiment (ACE), also known as Scisat, is a Canadian satellite-based mission for remote sensing of the Earth's atmosphere that has been collecting measurements since February 2004 [1]. The mission employs the solar occultation measurement technique, collecting a series of measurements through the Earth's atmosphere as tha Sun rises or sets from the orbiting satellite's perspective, providing up to 30 measurement opportunities per day. The primary instrument on board is the Atmospheric Chemistry Experiment Fourier transform spectrometer (ACE-FTS), featuring high resolution (0.02 cm^{-1}, unapodized), broad spectral coverage (750 to 4400 cm^{-1}), and a signal-to-noise ratio ranging from ~100:1 up to ~400:1 [1,2]. There is also a pair of filtered imagers on board, providing atmospheric extinction profiles at 527.11 and 1020.55 nm [1]. For both the ACE-FTS and the imagers, updates have been made to transmittance calculations and to retrievals, improving on previous processing versions [3–6].

2. ACE-FTS transmittances

Interferograms collected by the ACE-FTS instrument are converted to spectra using software provided by ABB, the instrument provider. 'Level 1′ data for the ACE-FTS instrument (geolocated atmospheric transmittance spectra) are then calculated by calibrating atmospheric measurements with averaged 'high sun' data (solar measurements taken above the altitude region where atmospheric constituents are expected to contribute significantly to the infrared spectrum). Both high sun and atmospheric spectra are corrected for self-emission by subtracting an average of spectra measured with the instrument pointed at a very cold target (deep space). High sun and deep space measurements are collected for each occultation (i.e., each sunrise or sunset event).

The ACE-FTS instrument has two detectors, one measuring the low wavenumber portion of the spectrum (750-1810 cm^{-1} in previous processing versions) and the other detector measuring the high wavenumber portion (1810-4400 cm^{-1} in previous processing versions). In order to improve the signal-to-noise ratio near 1810 cm^{-1}, the crossover point was moved to 1832.5 cm^{-1}, as shown in Fig. 1. Note that the dots in Fig. 1 are the measured spectral points, sampled at 0.02 cm^{-1}, and the downward pointing narrow lines are solar spectral features (absorption features from the Sun itself).

There was also a change to the procedure used to interpolate the final transmittance spectrum to the standard 0.02 cm^{-1} grid spacing, which involved balancing the sinc (sinx/x) interpolation kernel, yielding improved fidelity with a smaller number of points. Version 4 transmittances averaged high sun and deep space measurements over ± 3 orbits to reduce noise. For version 5, this was reduced to ± 1 orbit, trading a very small increase in noise levels for the reduced potential of systematic errors if the high sun measurement is changing (e.g., if a sunspot moves through the instrument's field of view).

* Corresponding author.
E-mail address: cboone@scisat.ca (C.D. Boone).

https://doi.org/10.1016/j.jqsrt.2023.108749
Received 15 June 2023; Received in revised form 3 August 2023; Accepted 5 August 2023
Available online 6 August 2023
0022-4073/

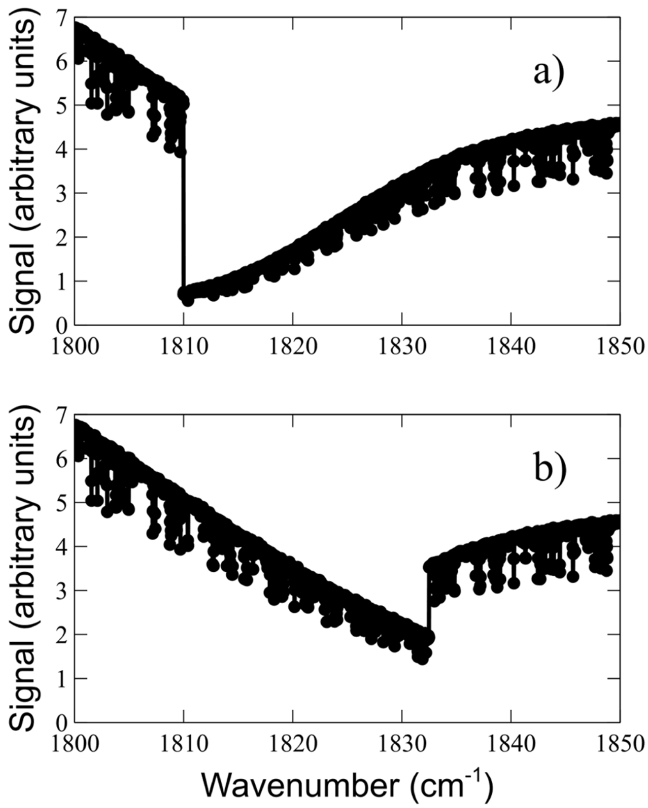

Fig. 1. Raw high sun spectrum from ss106550 (where ss stands for sunset, and 106,550 is the orbit number, creating a unique identifier for the occultation) in the vicinity of the crossover between the two ACE-FTS detector regions. The spectrum for wavenumbers below the step in the signal comes from one detector, while the spectrum above the step comes from the other detector. (a) Version 4. (b) Version 5.

3. ACE-FTS changes

3.1. Averaging over the field of view

The major change in version 5 processing is an averaging across the ACE-FTS field of view (FOV) rather than using a single ray in the center of the FOV for forward model calculations. To average across the FOV, we perform forward model calculations for a set of angular displacements from the FOV center, where the angular displacements are an integer times the unit displacement, Δθ, shown in Fig. 2 and are perpendicular to the Earth's horizon. The horizontal chords in Fig. 2 indicate the width of the circular FOV at the given displacement and are used to weight the average: the longer the horizontal chord, the greater the contribution to the average. If there are 2n+1 rays across the FOV included in the average, the weighting of ray *i* (where the index *i* is in the range from -n to +*n*) can be calculated as follows:

$$weighting(i) = cos\left(sin^{-1}\left(\frac{i}{n+1}\right)\right) \Big/ \sum_{j=-n}^{n} cos\left(sin^{-1}\left(\frac{j}{n+1}\right)\right)$$

The example shown in Fig. 2 corresponds to 11 rays ($n = 5$). For version 5 processing, 21 rays are averaged across the field of view ($n = 10$).

The 1.25 mrad diameter input aperture of the ACE-FTS corresponds to a 3–4 km altitude range at the tangent point (the location of closest approach to the Earth's surface for a measured solar ray), a relatively small footprint on the 25+ km span of the solar disk, as seen from the satellite. However, the peaked nature of the weighting function in the right panel of Fig. 2 indicates that the effective 'altitude resolving power' of the instrument is better than 3-4 km, something closer to 2-3 km.

The increased altitude smearing inherent in the calculation from averaging over the field of view necessitates an increase in the minimum altitude separation between volume mixing ratio (VMR) retrieval grid points [5] in order to suppress unphysical oscillations in the retrieved profiles. Above 15 km, the minimum altitude spacing for VMR retrieval grid points was 2.5 km for version 5 processing (up from 2.0 km in version 4). Below 15 km, the minimum spacing was 1.5 km (up from 1.0 km in version 4). For version 5 pressure/temperature (P/T) retrievals, no change was made to the minimum altitude grid spacing implemented in version 4 (2.0 km spacing above 19.5 and 1.5 km spacing below 19.5 km).

3.2. Changes to input data

For P/T retrievals, shapes of the pressure and temperature profiles above the highest analyzed measurement (~125 km) are derived from the empirical MSIS model provided by the U.S. Naval Research Laboratories [3]. Previous processing versions made use of the NRL-MSISE-00 version of the software [7]. ACE-FTS version 5 processing employs a newer version of the software: MSIS 2.0 [8].

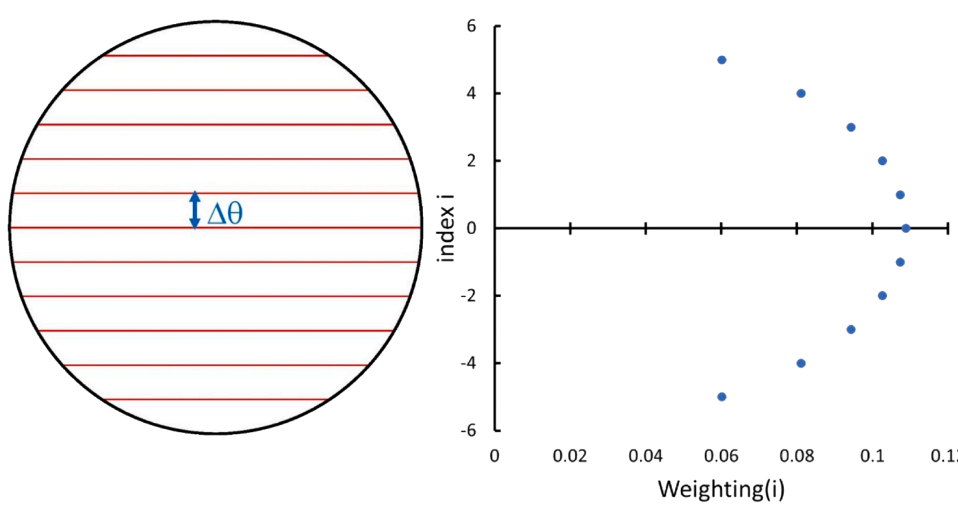

Fig. 2. Geometry for calculating average signal across the ACE-FTS FOV. The circle on the left represents the instrument's 1.25 mrad diameter input aperture. Horizontal lines represent locations within the FOV employed in the averaging, vertically offset from FOV center and separated by angle Δθ. The lengths of the lines are used to calculate the weighting in the average from each location. The calculated weighting for each line is shown in the plot on the right.

Spectroscopic data for version 5 were taken from HITRAN 2020 [9]. This includes updated line-by-line parameters for atmospherically significant molecules such as O_3, H_2O, and CO_2. Of particular interest is a ~2% change in O_3 intensities compared to the previous version of the line list [10]. Updates in HITRAN 2020 also include newly available cross section information for heavier molecules such as HFC-134a [11].

As with the previous processing version [5], non-Voigt line shapes such as speed-dependent Voigt and line mixing [12,13] for a number of CH_4 and N_2O lines are used in the region of the N_2 continuum, which is employed to determine tangent heights at low altitude [14]. Non-Voigt parameters are also used for CH_4 and N_2O lines overlapping the broad N_2O_5 spectroscopic feature in the wavenumber region 1225-1260 cm^{-1} [5]. These non-Voigt parameters were determined from analysis of ACE-FTS spectra.

3.3. Changes to existing retrievals

3.3.1. Pressure/temperature

P/T retrievals for the ACE-FTS are based on the analysis of CO_2 lines. Relative intensities of CO_2 lines with different lower state energies provide information on temperature (via different lower state populations), while absolute intensities provide information on pressure [3]. To expedite processing, microwindows (small portions of the spectrum containing spectral features from the target molecule with minimal 'pollution' from other molecules) are analyzed rather than analyzing entire spectra. Microwindows for the P/T retrieval were selected to contain CO_2 lines with a large as possible range of lower state energies at every altitude. However, in version 4, all the lines employed in the retrieval near 85-90 km had strong temperature sensitivity (i.e., large lower state energies). Using a single set of microwindows that would be applicable to all conditions excluded CO_2 lines with low temperature sensitivity (i.e., smaller lower state energies) in this altitude region: all candidate main isotopologue CO_2 lines of sufficient absorption strength would have been saturated (experienced completed absorption near line center) near 85-90 km for typical atmospheric conditions.

In the polar region near summer solstice, temperatures get extremely cold at the mesopause (near 90 km), leading to the formation of polar mesospheric clouds (PMCs) [15]. In version 4 processing, the temperature-sensitive CO_2 lines contained in the microwindows near 90 km often had extremely low absorption when measuring occultations containing PMCs. Fig. 3 shows the measured spectrum near 90 km for ss80363, an occultation where PMCs are observed, compared to the spectrum near 90 km for sr10063, where mesospheric temperatures are closer to normal. The rapid decrease in absorption strength for lines above ~2380 cm^{-1} caused significant difficulties in the version 4 processing, yielding fitted temperatures that were too low and spikes near 90 km in retrieved VMR profiles.

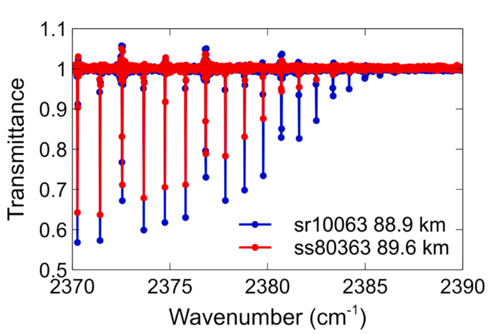

Fig. 3. The wing of the CO_2 ν_3 R-branch in measurements near tangent height 90 km. Plotted in blue is the spectrum for occultation sr10063 (where sr stands for sunrise), measured June 25th 2005 at latitude 37.6°S and longitude 161.4°E with a retrieved mesopause temperature of -177 K near 94 km. Shown in red is the spectrum for occultation ss80363, measured July 13th 2018 at latitude 67.8°N and longitude 43.9°E with a retrieved mesopause temperature of -127 K near 90 km. In this wavenumber region, the lower state energy of CO_2 lines in the spectra increases with increasing wavenumber. The extremely low temperature in ss80363 causes absorption strength to drop off rapidly for CO_2 lines above ~2380 cm^{-1}.

For version 5 P/T retrievals, the lower altitude limits for selected microwindows were made adjustable by having the software detect the lowest altitude for which the CO_2 line(s) in the given microwindow avoids saturation effects near line center. Thus, stronger lines (such as those near 2375 cm^{-1} in Fig. 3) contribute to the retrieval near 90 km in ss80363, rather than just the extremely weak lines near 2385 cm^{-1}. This avoids a severe under-constraint near 90 km for occultations with PMCs and will also improve the results in that altitude region for many occultations that do not contain PMCs by generally using more CO_2 lines in the analysis than was used in version 4. The microwindows used in the v5 retrieval are available on the ACE data distribution website in the ACE document ACE-SOC-0038: https://databace.scisat.ca/level2/ace_v5.2/ACE-SOC-0038-ACE-FTS_Spectroscopy-version_5.x.pdf.

3.3.2. Volume mixing ratios

For molecules that also appeared in version 4, the only changes to microwindow sets for version 5 were for ClO and SO_2 (all v5 microwindows are available in the ACE document cited above). The upper altitude limits for both molecules were pushed higher, and the lower altitude limit for SO_2 was raised. Contrary to initial expectations prior to version 4 processing, these two molecules appear to provide viable results even under background conditions [5,16] despite weak contributions to spectrum when at background levels.

SO_2 was retrieved to higher altitude to capture an apparent increase in VMR at higher altitudes, likely resulting from evaporation of sulfate aerosols at altitudes above the Junge layer [17]. The increased altitude range for this molecule is illustrated in Fig. 4, showing a (noisy) VMR peak near 35-40 km for the v5.2 profile. The error bars in Fig. 4 depict the random fitting errors from the least squares analysis (the square root of the diagonal elements of the covariance matrix). The relatively large random errors found in single profiles can be mitigated through modest averaging prior to scientific analysis.

ClO was pushed higher in an effort to capture the stratospheric VMR peak for the molecule [18]. Results near the upper altitude limit of the retrieval (40 km) are extremely noisy, suggesting difficulties in the retrievals in this altitude region. As such, the utility of the increased altitude range in version 5 remains to be evaluated.

3.4. New retrievals

3.4.1. HFC-32 (CH_2F_2)

The version 5 microwindow set employed for HFC-32 was reported

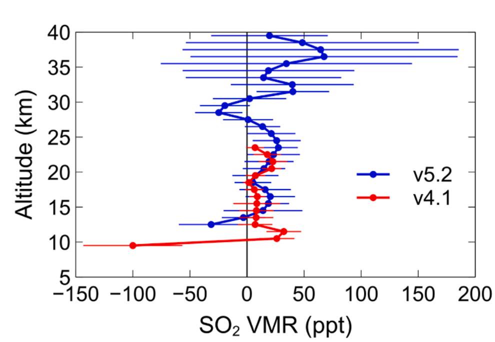

Fig. 4. Versions 4.1 (in red) and 5.2 (in blue) VMR profiles in parts per trillion (ppt) for SO_2 from occultations sr10063 (details of this occultation provided in the caption to Fig. 3). Error bars represent the random fitting errors from the least squares analysis. Both the lower and upper altitude limits were raised in version 5 processing for SO_2.

in a study of preliminary results for the molecule [19]. The retrieval employs a broad HFC-32 spectral feature near 1090 cm^{-1}. Fig. 5 presents the retrieval results from the high Arctic for 2008 and 2022. Atmospheric HFC-32 levels are increasing rapidly with time, as is evident from the differences between Figs. 5a and b. Provided in Fig. 5 is an estimate of HFC-32 VMR determined by the ground-based Advanced Global Atmospheric gases Experiment (AGAGE) [20] for the given time period in the Northern Hemisphere. In 2008 (Fig. 5a), levels are extremely low, and ACE-FTS results are biased slightly high, as was noted in Dodangodage et al., 2021. By 2022, there is good agreement between ACE-FTS tropospheric results and AGAGE surface observations (~39 ppt). This suggests a systematic effect in the analysis that reduces in significance over time as the strength of the HFC-32 spectral feature grows due to its rapidly increasing concentration. In Fig. 5b, the VMR decline above the tropopause (~9 km) results from chemical and photolysis losses combined with age of air.

Even in 2022, HFC-32 remains a relatively weak absorber in ACE-FTS spectra. Thus, the results exhibit relatively high variability, meaning it is useful to apply filtering and averaging in scientific analysis.

3.4.2. HOCl

The version 5 microwindow set employed for HOCl was reported in a study of preliminary results for the molecule [21]. The retrieval uses HOCl spectral features in the 1220 to 1260 cm^{-1} region. Fig. 6 shows HOCl profiles from July-September 2022 for two different latitude regions. Fig. 6a shows the results for northern midlatitudes. HOCl in this region is at background levels, yielding relatively high variability due to weak absorption in ACE-FTS spectra, making filtering and averaging a benefit for scientific analysis under background conditions. As seen from the average profile in Fig. 6a (in red), ACE-FTS results extend up to the VMR peak near 40 km [22] but not above the peak. With no constraints applied in ACE-FTS retrievals, attempts to push HOCl analysis higher would introduce large oscillations in some profiles. Fig. 6b corresponds to Antarctic winter, where chlorine processing on polar stratospheric cloud particles generates significant enhancements in HOCl for altitudes in the vicinity of 20-25 km [21], enhancements the order of 1 part per billion (ppb). HOCl enhancements have also been observed in chemical processing on stratospheric smoke particles [23].

3.4.3. Line of sight winds

Another new data product in ACE-FTS v5 processing is line of sight winds. Motion of molecules in the atmosphere relative to the satellite induces a Doppler shift in the measured spectrum, stretching or compressing the spectrum's wavenumber scale, depending on the direction of relative motion. The procedure for determining wind speed profiles from ACE-FTS measurements is described in detail in a separate study [24]. Basically, for each ACE-FTS measurement above 18 km, wavenumber shifts relative to a reference spectrum are determined for a collection of unsaturated lines, from which the wind velocity along the line of sight (v) can be calculated [24]:

$$v = c\frac{\Delta\sigma}{\sigma},$$

where c is the speed of light, σ is wavenumber, and Δσ is the Doppler-induced wavenumber shift. The instrument's look angle relative to geodetic north is provided at tangent heights 30 and 100 km to permit calculation of the component along the ACE-FTS line of sight from coincident vector (zonal and meridional) wind measurements [24].

Fig. 7 shows example wind speed profiles for two different atmospheric conditions: Arctic winter and Antarctic summer. The results in Fig. 7a probe winds within the polar vortex from multiple angles, yielding high variability in the stratosphere (below ~55 km). Stratospheric winds are much less variable in the Antarctic summer results in Fig. 7b, but winds in the thermosphere (above ~90 km) in this example exhibit extreme variability. In both cases, winds in the mesosphere (between ~55 and ~90 km) are relatively stable from occultation to occultation.

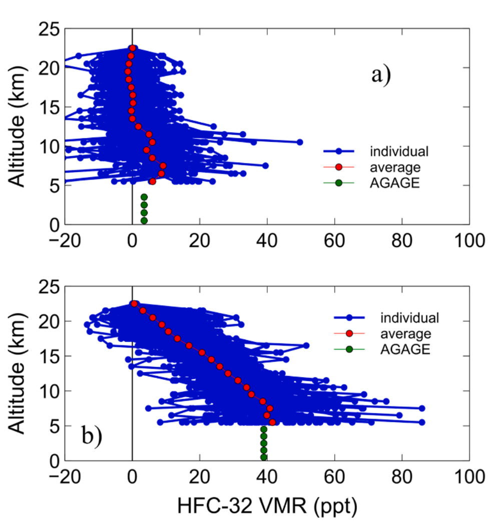

Fig. 5. ACE-FTS v5.2 HFC-32 retrievals for the latitude range 75 to 85°N from September and October. Individual profiles for the given year are shown in blue, average profiles are shown in red, and the estimated surface VMR from Northern Hemisphere sites in the ground based AGAGE network is shown in green. (a) results from 2008. (b) results from 2022.

4. ACE-imager changes

Although the imagers provide a full image of the Sun, to simplify the analysis transmittances (atmospheric transmission divided by the high sun signal) are only generated for pixels near the center of the ACE-FTS field of view. This permits the use of geometry information derived from ACE-FTS analysis results for altitude registration of the imager transmittance data.

Rows in the 'native' images are oriented at an angle to the horizon [25]. Prior to analysis, a cubic convolution rotation [26] about the given imager's sun centroid is applied to generate an image with rows parallel to the horizon [25]. In version 5 processing, the image is first interpolated onto a fine grid before applying the rotation. This ensures optimal mapping of fine details in the rotated image.

Previous processing versions averaged results for 3 pixels in the row coincident with the center of the ACE-FTS FOV. For version 5 processing, the number of pixels averaged was increased to 5 to reduce noise. Also, transmittances were calculated for the adjacent row of pixels below the row at the ACE-FTS FOV center, offset by 0.234 μrad. This doubles the fitting data, which should improve retrieved extinction profiles. Because the two rows are offset in altitude, the impact of transient aerosol plumes or clouds passing rapidly through the imager field of regard will be suppressed in the extinction profile. The extra row of pixels also extends imager retrievals slightly lower in altitude.

In previous processing versions, imager extinction profiles would occasionally have a large offset at high altitude (i.e., would not tend toward zero extinction at high altitude). In version 5, this was fixed by identifying and removing contributions to the calculated high sun average signal that were actually from deep space measurements (and therefore had a signal near zero). Also, transmittances were refined by recalibrating to ensure the average transmittance above 100 km was equal to 1, because negligible extinction is expected for that altitude region.

Fig. 8 shows example aerosol extinction profiles from both imagers for a particular occultation (sr86637). Aerosol extinction is atmospheric extinction minus contributions from Rayleigh scattering and the weak absorption from gas phase molecules [6]. Comparisons are made to corresponding channels from the Stratospheric Aerosol and Gas

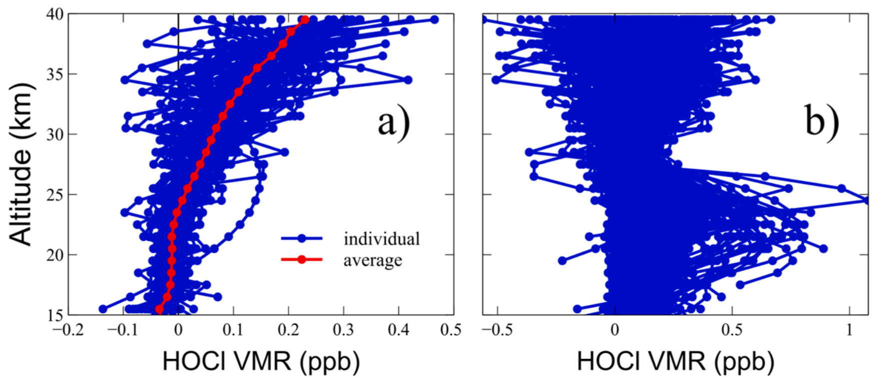

Fig. 6. ACE-FTS v5.2 HOCl results for July through September 2022. (a) Latitudes 45-60°N, with profiles from ~100 individual occultation shown in blue and the average profile shown in red. (b) Latitudes 60-80°S, with ~900 individual profiles plotted in blue. Frequent enhancements are observed in the 20-25 km altitude range. Note the different horizontal scales.

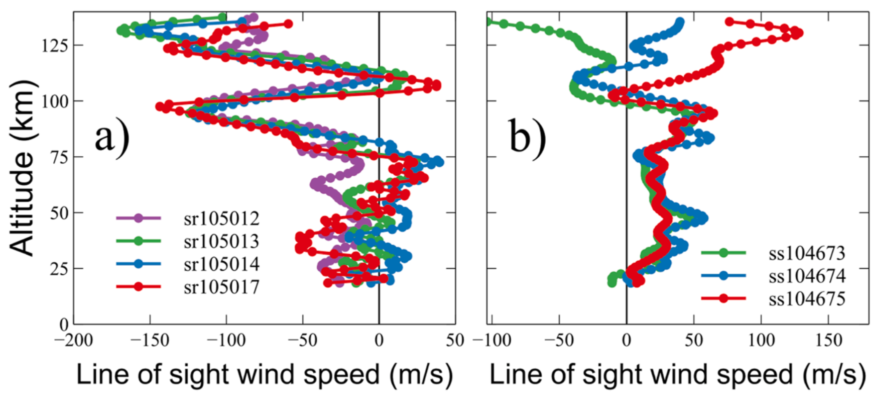

Fig. 7. V5.2 line of sight winds for different atmospheric conditions. (a) A set of occultations in Arctic winter from February 7th, 2023, near latitude 67.3°N. b) A set of consecutive occultations in Antarctic summer from January 15th, 2023, near latitude 68.2°S.

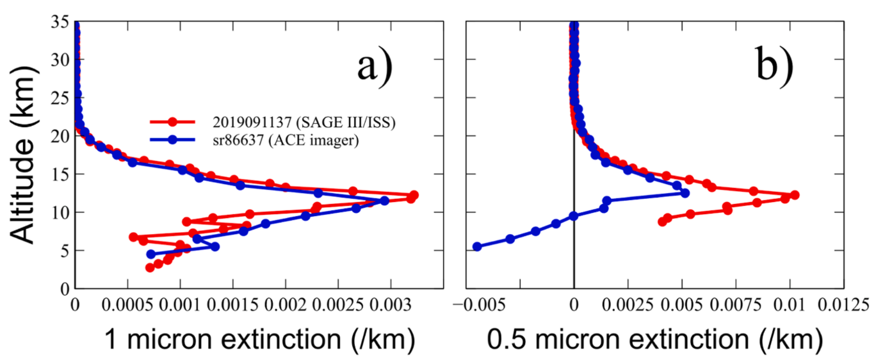

Fig. 8. Comparisons between aerosol extinction profiles from v5.2 ACE-imager results and v5.3 results from SAGE III/ISS for coincident occultations: sr86637 (September 11th, 2019, latitude 58.0°N, longitude 157.4°E) from ACE and event 2019091137 from SAGE III/ISS, with a 3-point running average applied to SAGE results to reduce variability. (a) Results at 1.02 μm for ACE imager and SAGE III/ISS. (b) Results at 0.527 μm for ACE imager and 0.521 μm for SAGE III/ISS.

Experiment III instrument on the International Space Station (SAGE III/ISS) [27], with a 3-point running average applied to the SAGE results to reduce its high variability. The two coincident measurements are separated by roughly 2 min, 0.2° in latitude and 0.4° in longitude.

There is relatively good agreement for the 1-micron results, with some evidence of a small altitude offset. For 0.5 μm, ACE-imager results are biased low, going negative at the lowest altitudes. This is a common occurrence for the 0.5-micron ACE-imager and suggests the presence of unexpected extra light falling on the detector at low altitudes. The likely source is light 'leaking' around the filter that provides wavelength discrimination. At higher altitudes, this leakage provides a small signal relative to that from the Sun. Moving to lower altitudes, the leakage signal becomes a larger and larger percentage of the total signal for the 0.5-micron imager and likely dominates the signal for tangent heights near 5 km. Therefore, the 0.5-micron ACE-imager is not recommended for quantitative analysis.

5. Versions 5.0, 5.1, and 5.2

The initial release of the new processing version (v5.0) exhibited excessive variability in VMR retrieval results for occultations prior to 2011. This was traced back to a change in operating environment for the supercomputing cluster on which the processing was run. This problem was easily addressed by simply recompiling the software and reprocessing affected (i.e., pre-2011) occultations. Additionally, a small percentage of occultations throughout the mission had unphysical spikes near 30 km in the VMR profiles of all molecules. This resulted from the P/T retrieval converging to a local minimum in χ^2 for the nonlinear least squares fitting. For some (but not all) occultations experiencing this problem, relatively simple changes in initial guess parameters for the P/T retrieval permitted the software to converge to the global χ^2 minimum.

A new processing version (v5.1) was generated by reprocessing occultations prior to 2011 and occultations identified as having spikes near 30 km, using software with the updated approach for generating initial guess parameters for the P/T retrieval. No other changes were made to the software. Versions 5.0 and 5.1 results are identical for occultations that did not have spikes near 30 km (these occultations were not reprocessed). This expedited the new data product, avoiding the 6-to-8-month time frame required to reprocess the entire mission. The use of selective processing does not impact the internal consistency of v5.1 because changing the initial guess parameters in the P/T retrieval induces negligible differences in the retrieval results for occultations that did not have spikes near 30 km (i.e., occultations that did not get stuck in a local χ^2 minimum).

As mentioned previously, the change in initial guess parameters did not fix the convergence problem for all occultations. A robust treatment of the convergence problem would require significant changes in the software, which in turn would necessitate reprocessing the entire mission to maintain an internally consistent processing version. The spikes near 30 km are unphysical artifacts and should not be used for scientific analysis. Therefore, a new processing version (v5.2) was generated that excludes occultations having a spike near 30 km in v5.1, identified by N_2 results having VMR $\geq$ 0.95 in the altitude range 27 to 37 km. Fig. 9 shows v5.1 N_2 VMR profiles from November 2022, with profiles that were included in v5.2 shown in blue and profiles with spikes near 30 km (and therefore excluded from v5.2) shown in red.

Over the span of the mission up to the end of May 2023, 1593 occultations with spikes near 30 km were excluded from v5.2, roughly 1.3% of the total. Most of these occultations will be recovered in a future processing version that provides a robust fix for the intermittent convergence problem in P/T retrievals.

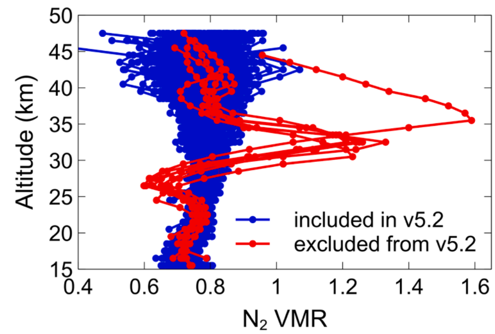

Fig. 9. Retrieved v5.1 N_2 VMR profiles from November 2022. In blue are profiles from 700 occultations that are included in v5.2. In red are 8 profiles with spikes near 30 km, resulting from convergence problems in the v5.1 P/T retrievals, from occultations that have been excluded from v5.2.

6. Conclusions

Version 5 of ACE-FTS processing provides line of sight winds and VMRs for two new molecules: HFC-32 and HOCl. For the first time, the ACE-FTS field of view is modeled in the analysis. MSIS 2.0 is used to calculate the shape of pressure and temperature profiles above the highest analyzed measurements in the P/T retrieval (~125 km). Spectroscopy is taken from the latest edition of HITRAN: HITRAN 2020. A variable lower altitude limit was implemented on selected microwindows in the P/T retrieval in order to avoid large systematic errors near the mesopause during PMC season.

Version 5 of ACE-imager processing uses more data from the imager in the retrieval and fixes transmittance errors from deep space measurements misidentified as high sun in previous processing versions.

The recommended processing version for scientific analysis is v5.2, which excludes a small percentage of occultations from v5.1 that contain unphysical artifacts. This does not remove occultations that experienced problems from other issues, such as large altitude gaps resulting from data lost during transmission from the satellite to the ground. Filtering of the data may still be required in some situations.

Data availability

ACE-FTS data can be accessed at the following web portal: https://databace.scisat.ca/level2/ace_v5.2/display_data.php. First time data users can register at https://databace.scisat.ca/l2signup.php. SAGE data are available from NASA's Atmospheric Science Data Center (https://eosweb.larc.nasa.gov/). AGAGE data can be obtained from https://agage.mit.edu/data/agage-data.

Declaration of Competing Interest

The authors declare that they have no known competing financial interests or personal relationships that could have appeared to influence the work reported in this paper.

Acknowledgments

Funding is provided by the Canadian Space Agency (9F045–200575/001/SA). Thanks to Jeff Crouse for work on the imager retrievals and initial administration of v5.0 processing.

References

[1] Bernath PF. The atmospheric chemistry experiment (ACE). J Quant Spectrosc Radiat Transf 2016;186:3–16. https://doi.org/10.1016/j.jqsrt.2016.04.006.
[2] Buijs HL, Soucy MA, Lachance RL. ACE-FTS hardware and level 1 processing. the atmospheric chemistry experiment ace at 10: a solar occultation anthology. Hampton, VA, USA: A. Deepak Publishing; 2013. p. 53–80.
[3] Boone CD, Nassar R, Walker KA, Rochon Y, McLeod SD, Rinsland CP, Bernath PF. Retrievals for the atmospheric chemistry experiment Fourier-transform spectrometer. Appl Opt 2005;44(33):7218–31. https://doi.org/10.1364/ao.44.007218.
[4] Boone CD, Walker KA, Bernath PF. Version 3 retrievals for the Atmospheric Chemistry Experiment Fourier transform spectrometer (ACE-FTS). The Atmospheric Chemistry Experiment ACE at 10: a solar occultation anthology. Virginia: A Deepak Publishing; 2013. p. 103–27. edited by Peter Bernath.
[5] Boone CD, Bernath PF, Cok D, Jones SC, Steffen J. Version 4 retrievals for the atmospheric chemistry experiment Fourier transform spectrometer (ACE-FTS) and imagers. J Quant Spectrosc Radiat Transf 2020;247:106939. https://doi.org/10.1016/j.jqsrt.2020.106939.
[6] Vanhellemont F, Tetard C, Bourassa A, Fromm M, Dodion J, Fussen D, et al. Aerosol extinction profiles at 525nm and 1020nm derived from ACE imager data: comparisons with GOMOS, SAGE II, SAGE III, POAM III, and OSIRIS. Atmos Chem Phys 2008;8:2027–37. https://doi.org/10.5194/acp-8-2027-2008.
[7] Picone JM, Hedin AE, Drob DP, Aikin AC. NRLMSIS-00 empirical model of the atmosphere: statistical comparisons and scientific issues. J Geophys Res 2002;107 (A12):1468–83. https://doi.org/10.1029/2002JA009430.
[8] Emmert JT, Drob DP, Picone JM, Siskind DE, Jones Jr M, Mlynczak MG, et al. NRLMSIS 2.0: a whole-atmosphere empirical model of temperature and neutral species densities. Earth Space Sci 2021;8:e2020EA001321. https://doi.org/10.1029/2020EA001321.
[9] Gordon IE, Rothman LS, Hargreaves RJ, Hashemi R, Karlovets EV, Skinner FM, et al. The HITRAN2020 molecular spectroscopic database. J Quant Spectrosc Radiat Transf 2022;277:107949. https://doi.org/10.1016/j.jqsrt.2021.107949.
[10] Gordon IE, Rothman LS, Hill C, Kochanov RV, Tan Y, Bernath PF, et al. The HITRAN2016 molecular spectroscopic database. J Quant Spectrosc Radiat Transf 2017;203:3–69. https://doi.org/10.1016/j.jqsrt.2017.06.038.
[11] Harrison JJ. Infrared absorption cross sections for 1,1,1,2-tetrafluoroethane. J Quant Spectrosc Radiat Transf 2015;151:210–6. https://doi.org/10.1016/j.jqsrt.2014.09.023.
[12] Boone CD, Walker KA, Bernath PF. Speed-dependent Voigt profile for water vapor in infrared remote sensing applications. J Quant Spectrosc Radiat Transf 2007;105:525–32. https://doi.org/10.1016/j.jqsrt.2006.11.015.

[13] Boone CD, Walker KA, Bernath PF. An efficient analytical approach for calculating line mixing in atmospheric remote sensing applications. J Quant Spectrosc Radiat Transf 2011;112:980–9. https://doi.org/10.1016/j.jqsrt.2010.11.013.
[14] Boone CD, Bernath PF. Tangent height determination from the N_2 continuum for the atmospheric chemistry experiment fourier transform spectrometer. J Quant Spectrosc Radiat Transf 2019;238:106481. https://doi.org/10.1016/j.jqsrt.2019.04.033.
[15] Jones SC, Bernath PF, Boone CD. Properties of polar mesospheric clouds from ACE satellite infrared spectra. J Quant Spectrosc Radiat Transf 2019;238:106518. https://doi.org/10.1016/j.jqsrt.2019.05.029.
[16] Cameron WD, Bernath P, Boone C. Sulfur dioxide from the atmospheric chemistry experiment (ACE) satellite. J Quant Spectrosc Radiat Transf 2021;258:107341. https://doi.org/10.1016/j.jqsrt.2020.107341.
[17] Rinsland CP, Gunson MR, Ko MKW, Weisenstein DW, Abrams MC, Goldman A, et al. H_2SO_4 photolysis: a source of sulfur dioxide in the upper stratosphere. Geophys Res Lett 1995;22(9):1109–12. https://doi.org/10.1029/95GL00917.
[18] Froidevaux L, Kinnison DE, Santee ML, Millán LF, Livesey NJ, Read WG, et al. Upper stratospheric ClO and HOCl trends (2005–2020): aura Microwave Limb Sounder and model results. Atmos Chem Phys 2022;22:4779–99. https://doi.org/10.5194/acp-22-4779-2022.
[19] Dodangodage R, Bernath PF, Boone CD, Crouse J, Harrison JJ. The first remote-sensing measurements of HFC-32 in the Earth's atmosphere by the atmospheric chemistry experiment Fourier transform spectrometer (ACE-FTS). J Quant Spectrosc Radiat Transf 2021;272:107804. https://doi.org/10.1016/j.jqsrt.2021.107804.
[20] Prinn RG, Weiss RF, Arduini J, Arnold T, DeWitt HL, Fraser PJ, et al. History of chemically and radiatively important atmospheric gases from the advanced global atmospheric gases experiment (AGAGE). Earth Syst Sci Data 2018;10:985–1018. https://doi.org/10.5194/essd-10-985-2018.
[21] Bernath PF, Dodangodage R, Boone CD, Crouse J. HOCl retrievals from the atmospheric chemistry experiment. J Quant Spectrosc Radiat Transf 2021;264:107559. https://doi.org/10.1016/j.jqsrt.2021.107559.
[22] von Clarmann T, Glatthor N, Grabowski U, Hopfner M, Kellmann S, Linden A, et al. Global stratospheric HOCl distributions retrieved from infrared limb emission spectra recorded by the michelson interferometer for passive atmospheric sounding (MIPAS). J Geophys Res 2006;111:D05311. https://doi.org/10.1029/2005JD005939.
[23] Bernath P, Boone C, Crouse J. Wildfire smoke destroys stratospheric ozone. Science 2022;375:1292–5. https://doi.org/10.1126/science.abm5611.
[24] Boone CD, Steffen J, Crouse J, Bernath PF. Line-of-Sight Winds and Doppler Effect Smearing in ACE-FTS Solar Occultation Measurements. Atmosphere 2021;12(6):680. https://doi.org/10.3390/atmos12060680.
[25] Gilbert KL, Turnbull DN, Walker KA, Boone CD, McLeod SD, Butler M, et al. The onboard imagers for the Canadian ACE SCISAT-1 mission. J Geophys Res 2006;112:D12207. https://doi.org/10.1029/2006JD007714.
[26] Keys RG. Cubic convolution interpolation for digital image processing. IEEE Trans Acoust Speech Signal Process 1981;29:1153–60. https://doi.org/10.1109/TASSP.1981.1163711.
[27] Wrana F, von Savigny C, Zalach J, Thomason LW. Retrieval of stratospheric aerosol size distribution parameters using satellite solar occultation measurements at three wavelengths. Atmos Meas Tech 2021;14:2345–57. https://doi.org/10.5194/amt-14-2345-2021.